Supplementary Information:

Early stage structural development of prototypical zeolitic imidazolate framework (ZIF) in solution

Maxwell W. Terban,[1] Debasis Banerjee,[2] Sanjit Ghose,[3] Bharat Medasani,[2] Anil Shukla,[4] Benjamin A. Legg,[2] Yufan Zhou,[4] Zihua Zhu,[4] Maria L. Sushko,[2] Jim J. De Yoreo,[2,5] Jun Liu,[6] Praveen K. Thallapally,[2,*] Simon J. L. Billinge[1,7,*]

[1] Department of Applied Physics and Applied Mathematics, Columbia University, New York, NY 10027
[2] Fundamental and Computational Science Directorate, Pacific Northwest National Laboratory Richland, WA 99352
[3] National Synchrotron Light Source II, Brookhaven National Laboratory, Upton, NY 11973
[4] W. R. Wiley Environmental Molecular Sciences Laboratory, Pacific Northwest National Laboratory, Richland, Washington 99354, United States
[5] Department of Materials Science and Engineering, University of Washington, Seattle, WA, 98185
[6] Energy & Environment Directorate, Pacific Northwest National Laboratory, Richland, Washington 99354, United States
[7] Condensed Matter Physics and Materials Science Department, Brookhaven National Laboratory, Upton, NY 11973

I. Additional TEM Studies:

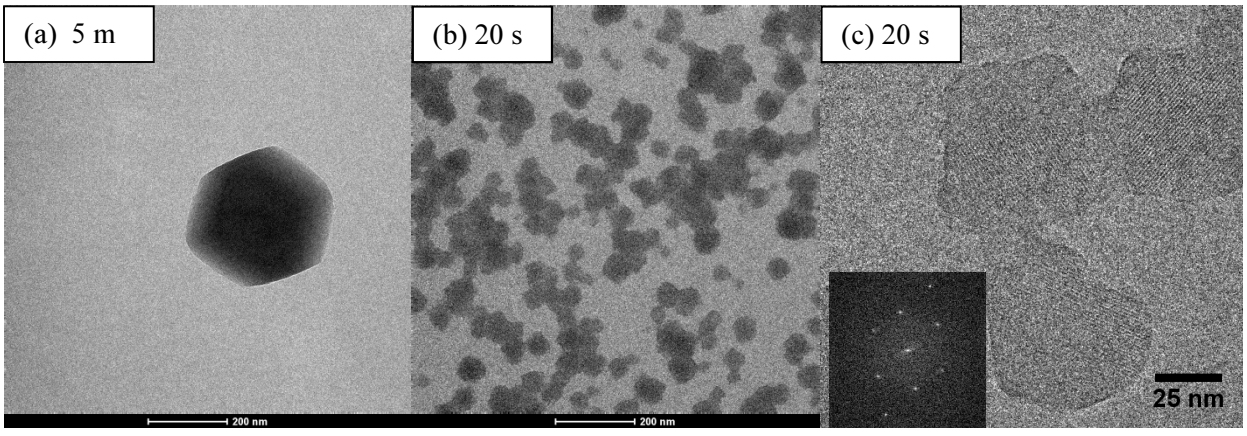

Fig S1: TEM images for the slowed reaction carried out at 0 °C using an ice-water bath, acquired after (a) 5 min and (b) 20 s. (c) Lattice fringes are clearly visible in a high-resolution image of the particles produced at 20 s aging, demonstrating that a crystalline component has already formed.

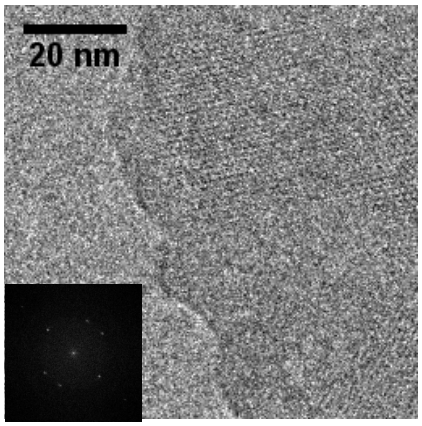

Fig S2: Alternate view of TEM image for the products formed by 20 s under the 0 °C reaction.

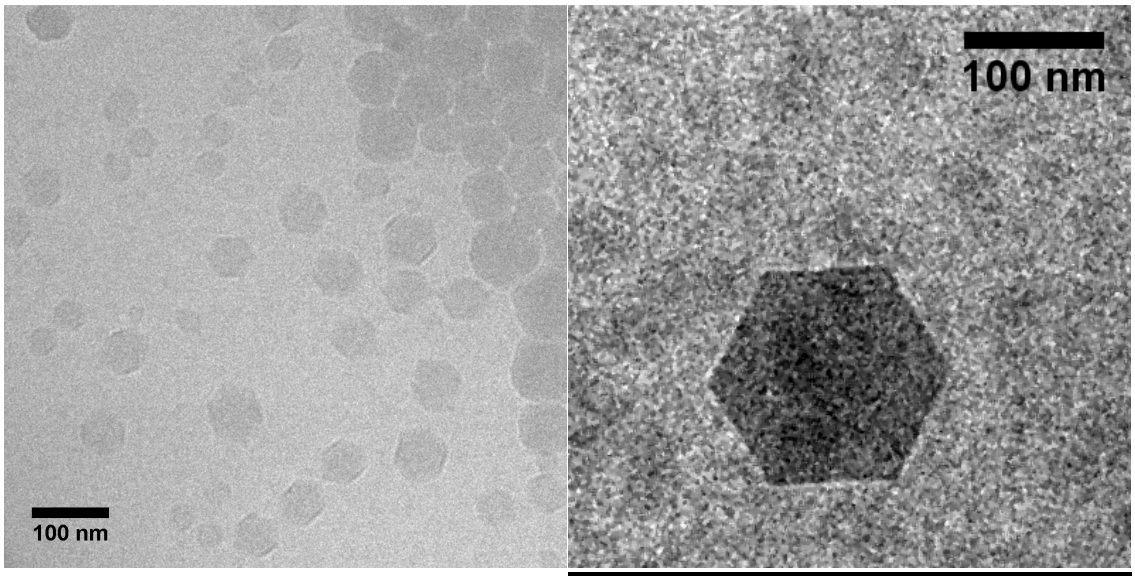

Fig S3: Cryo-TEM images of a sample aged for 25 h. The particle morphology is consistent with standard TEM measurements.

II. Reaction cell PDF experiments:

Initial *in situ* PDF measurements were performed in a static reaction cell at ratios of 1:2 and 1:6 (Zn:2-MeIm). The precursor solutions were injected to the cell, and measurements started approximately 2 minutes after injection. For the 1:6 case, Bragg peaks were observed at the earliest times measured, approximately 2 minutes after injection, and the subsequent PDFs contained both high and low frequency terms at high-*r,* similar to the ZIF-8 standard, indicating the presence of crystalline ZIF-8 particles. Qualitatively, no changes were observed up to 104 minutes of measurement, indicating that reaction is rapidly completed, in agreement with TEM measurements. For the 1:2 case, distinct Bragg peaks were not observed, though a slight increase in structural ordering was evident in the PDF up to 224 minutes. However, in both cases, low *Q*-resolution and poor signal-to-noise in the resulting PDFs with this apparatus prevented reliable tracking of the extent of crystallization or crystallite size in either reciprocal or real space.

Fig S4: Static reaction cell used for longer time experiments.

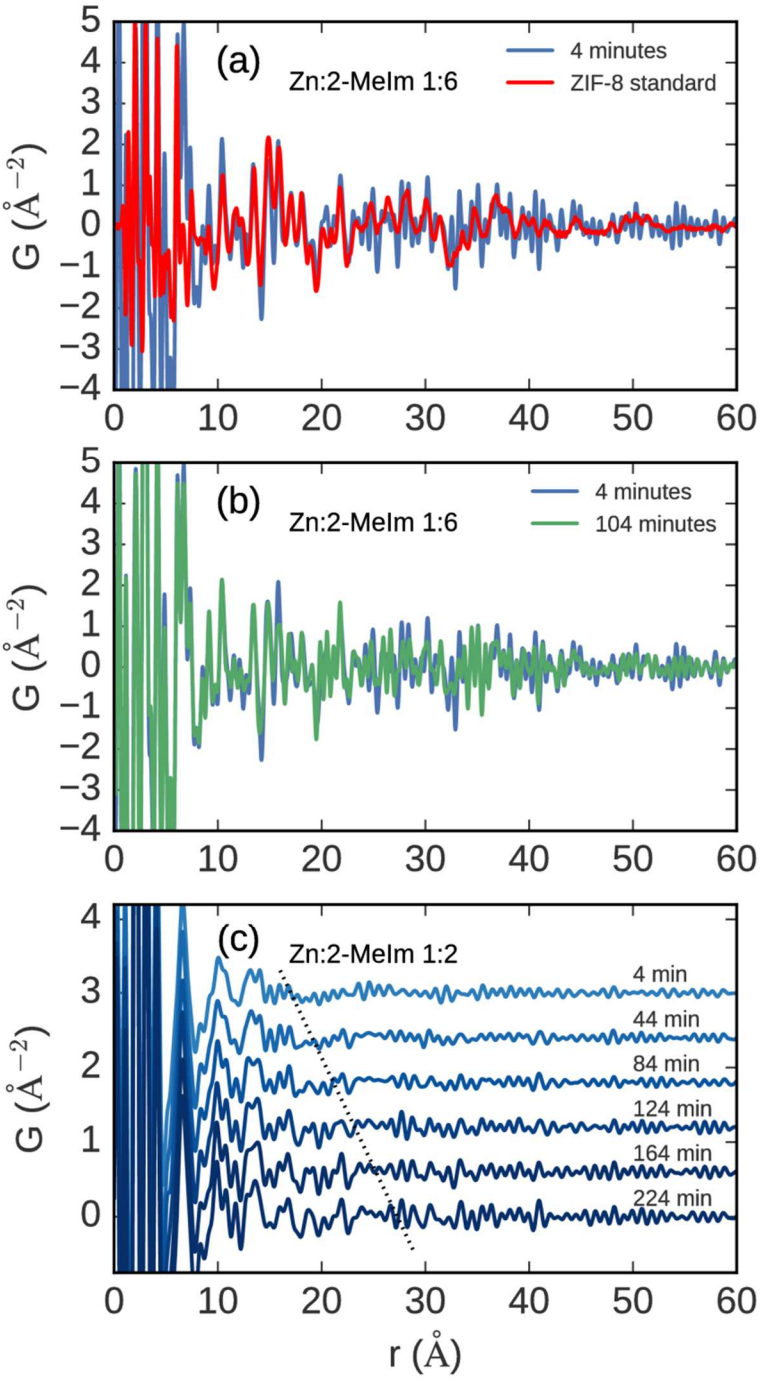

Fig S5: (a) The PDF measured from the 1:6 mixture in the reaction cell after 4 minutes compared to the PDF of the ZIF-8 standard, showing that long range ordered crystalline product has formed. (b) The PDFs from 4 and 104 minutes are overlayed, showing that the signal from the long-range ordered product has not evolved over this time period. (c) The PDFs from the 1:2.5 mixture are shown in increments from 4 to 224 minutes. Some changes are evident in the medium-*r* range. A dotted line is given as a guide to the eye for the appearance of new features in the signal at higher distances.

III. Flow cell PDF experiments:

To investigate the early stages of the reaction, we loaded the precursors into syringes and injected them into a reaction flow cell with a single outlet, allowing continuous flow of the product solution, such that the extent of reaction should remain constant in time at any given distance measured along the tube. We sought to slow down the reaction, without changing the temperature of the reagents, which was not possible in our setup. Two factors could be controlled to affect the extent of reaction in the measured signal: (a) measuring at different distances along the flow cell, and (b) changing the flow rate to change the residence time of the reactants. In our measurements, the beam could not be placed directly at the location where the inlets first mixed. We therefore tuned the flow rate of the inlets to change the relative extent of reaction at the same cell position. The pump rate was controlled using a Harvard Apparatus Pump 11 Elite. The cell consisted of a 2 mm ID Kapton tube to simultaneously increase the scattering statistics collected from a larger scattering volume and decrease background scattering from the cell. The precursor solutions consisted of zinc nitrate in H_2O and 2-MeIm in MeOH prepared such that the molar ratio on mixing varied between 1:2, 1:4, and 1:6 (Zn:2-MeIm) with theoretical product yields of 1, 3, or 5 wt%. The background was measured by pumping methanol and water without the reactants at a 1:1 ratio.

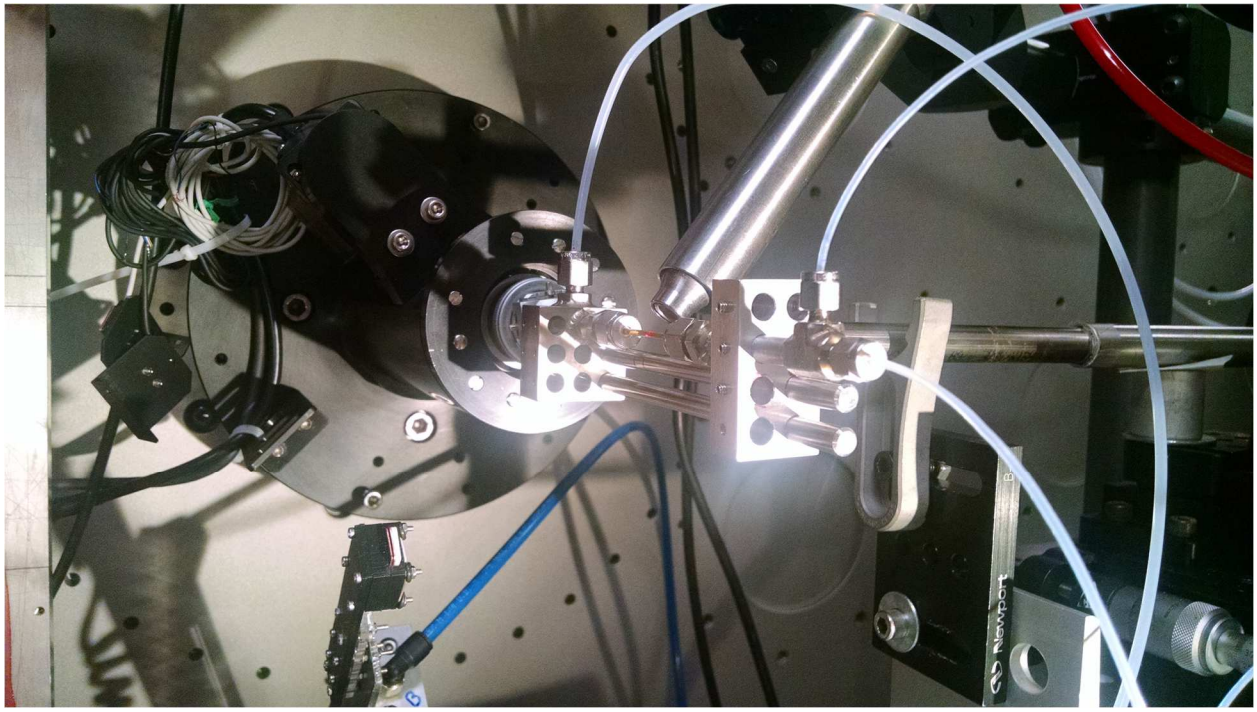

Fig S6: Flow cell used for *in situ* PDF measurements.

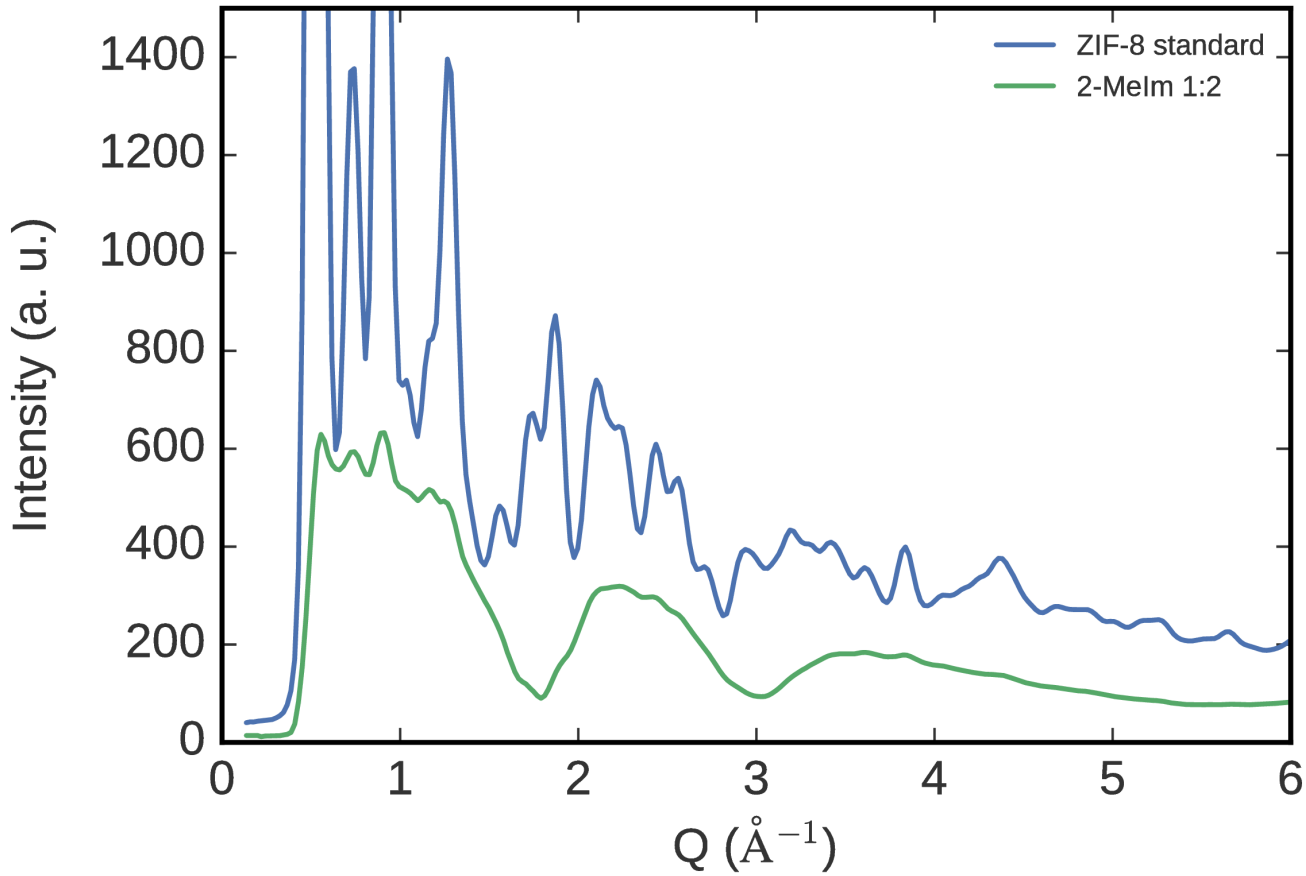

Fig. S7: Representative scattering intensities after background subtraction for a 1:2 ratio mixture measured in the flow cell. Some low intensity Bragg peaks are already observable at low-*Q*.

IV. PDF Modeling:

We employed visual comparison of PDF curves of the products and standards in order to determine the presence or absence of both short- and long-range ordered components. We fit the PDF of the standard ZIF-8 to the long-range ordered signal in the *in situ* products. A least squares fitting procedure was used to optimize the scaling of the ZIF-8 standard as well as an envelope function,[1] given by,

$$G_{product}(r) = \gamma_0(r) G_{standard}(r)$$

where γ_0 reflects the expected attenuation with increasing-*r* due to the effects from finite size and shape of the nanostructural domain of coherence (crystallite size). We used the characteristic function for a spherical domain which is given as,[2]

$$\gamma_0(r)_{sphere} = \left[1 - \frac{3r}{2d} + \frac{1}{2}\left(\frac{r}{d}\right)^3\right] H(d - r)$$

where *d* is the domain diameter, *H(r)* is a step function with value 1 for $r \leq d$ and 0 beyond.

In order to further verify the expected molecular and crystalline structural motifs, theoretical PDFs were simulated from atomic models and fit to the experimental PDFs by refinement of the model structure. For periodic crystal structures, *G(r)* was calculated from known structure models according to

$$G(r) = \frac{1}{rN} \sum_{i,j \neq i} \frac{f_i^* f_j}{\langle f \rangle^2} \delta(r - r_{ij}) - 4\pi\rho_0\gamma_0(r)$$

summed over all atoms in the model with periodic boundary conditions on the unit cell. N is the number of atoms, f_i and f_j are the x-ray atomic form factors of, and r_{ij} the distance between, atoms i and j, and ρ_0 is the average atom number density. In this case, the fitting program PDFgui[3] was used to carry out small box model refinements, by refining lattice parameters, scale factors, isotropic thermal displacement parameters U_{iso}, and peak sharpening coefficients to account for *r*-dependent correlated motion.[4]

For discrete molecular models, as in the case of the precursor molecules, the PDF was simulated using the Debye equation,

$$F(Q) = \frac{1}{N\langle f \rangle^2} \sum_i \sum_{j \neq i} f_i^* f_j \frac{\sin Q r_{ij}}{r_{ij}}$$

where the reduced total scattering structure function $F(Q) = Q[S(Q) - 1]$ is then Fourier transformed using the same sine Fourier transform used to process the experimental data,

$$G(r) = \frac{2}{\pi} \int_{Q_{min}}^{Q_{max}} F(Q) \sin(Qr)\, dQ$$

where Q_{min} and Q_{max} are the limits of the integration. This was implemented using Diffpy-CMI.[5]

V. Electrospray Ionization – Mass Spectrometry (ESI-MS) Data:

Experiments with zinc nitrate and 2-methylimidazole:

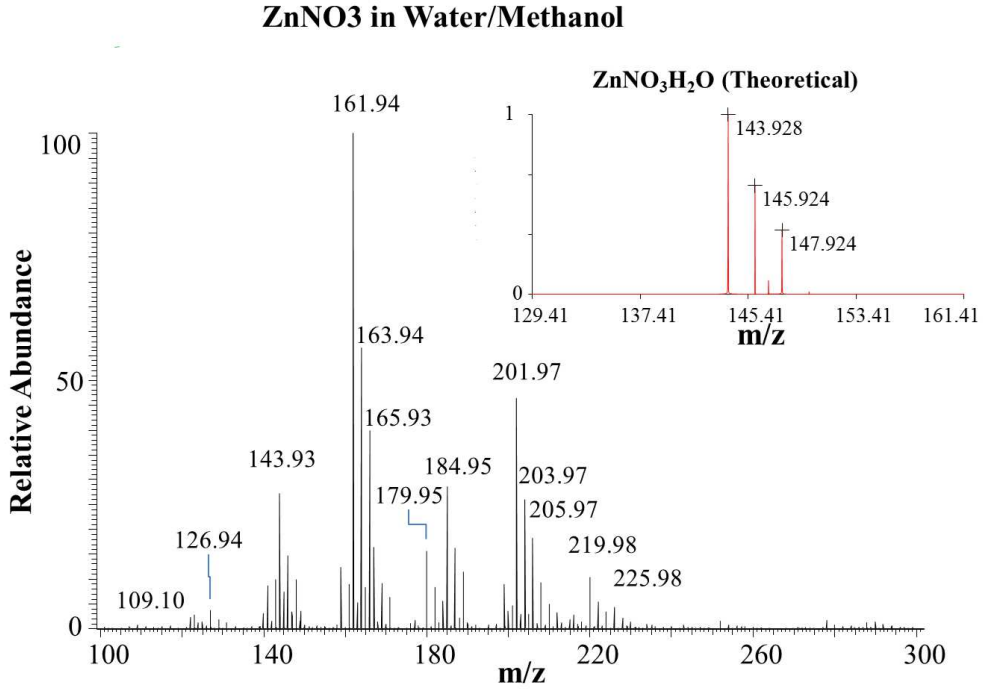

Fig. S8. ESI-MS spectra for $Zn(NO_3)_2 \cdot 6H_2O$ in water/methanol (1:1 v/v)

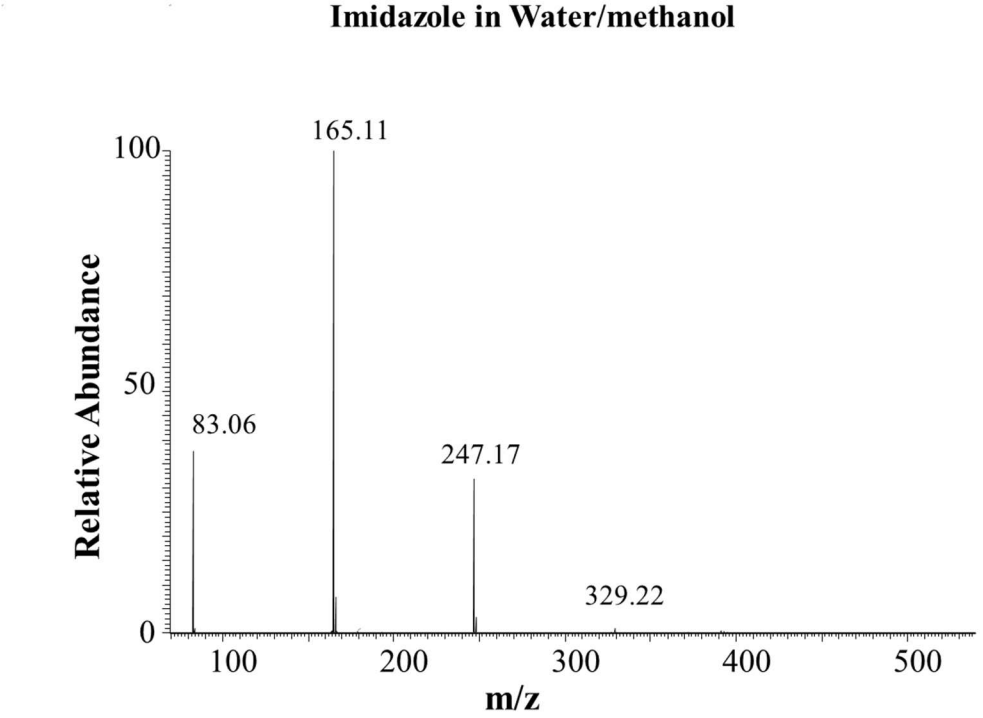

Fig. S9. ESI-MS spectra for 2-methylimidazole in water/methanol (1:1 v/v)

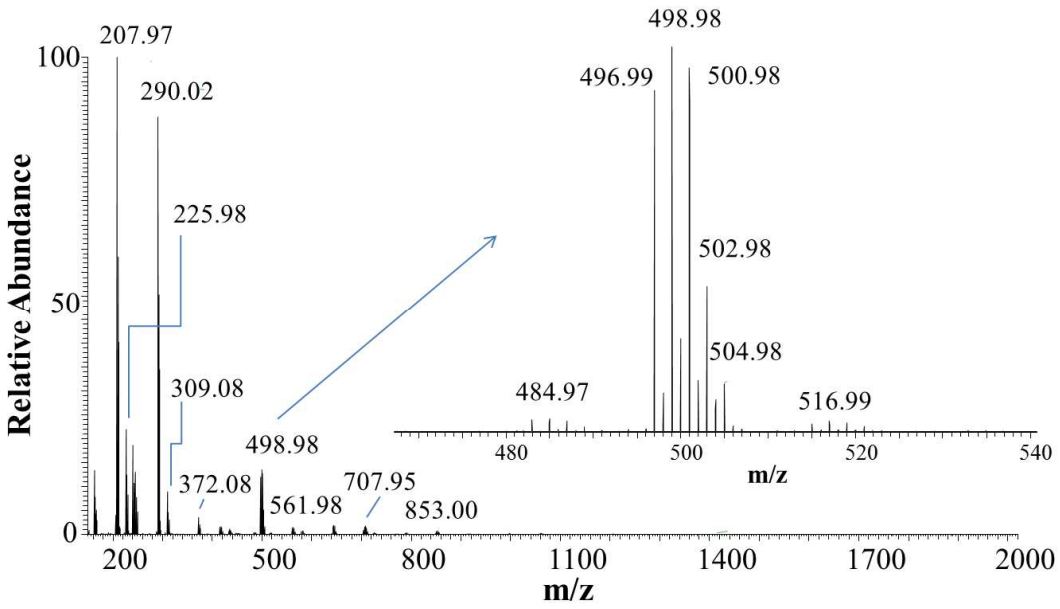

Fig. S10. Full ESI-MS spectrum of $Zn(NO_3)_2$ and 2-methylimidazole mixture (1:2 molar ratio) after 2 hours of mixing.

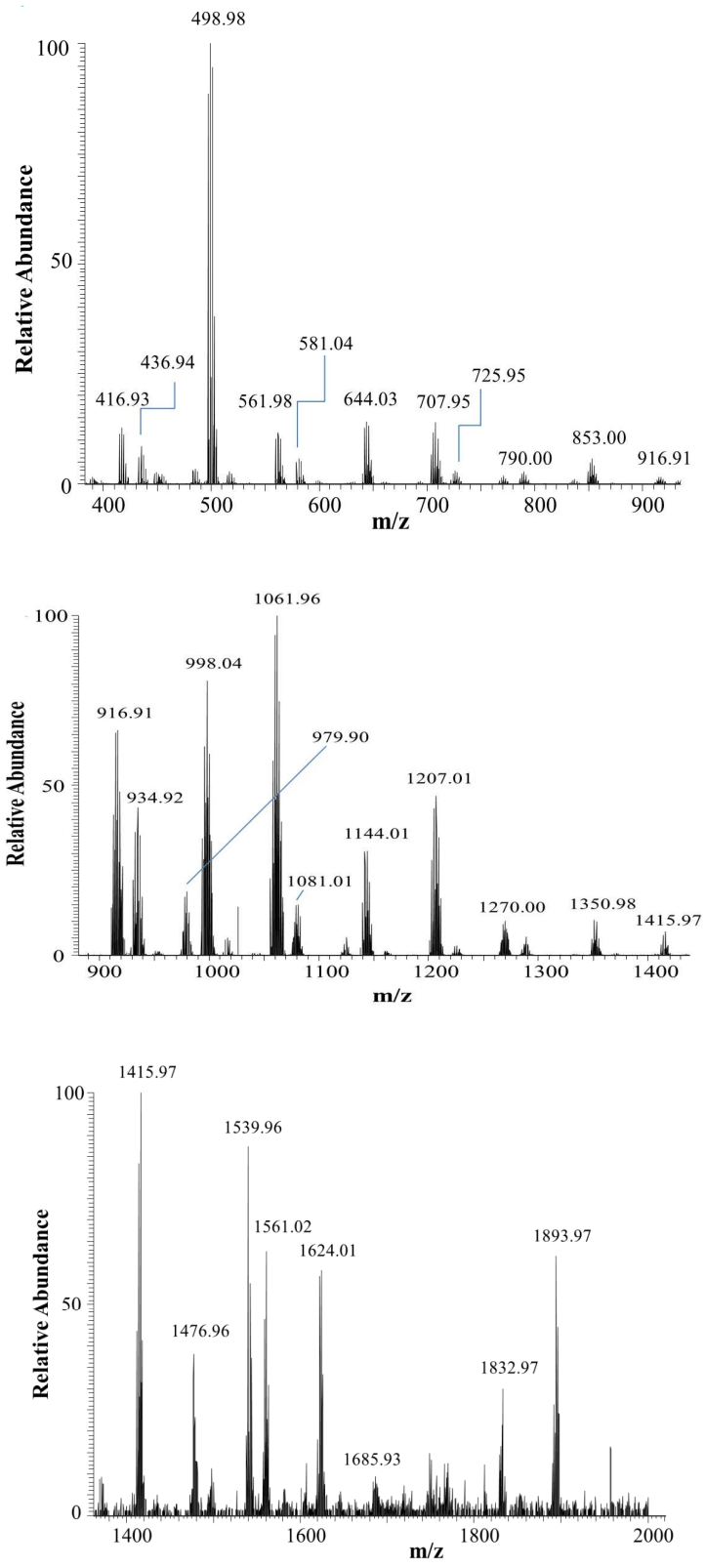

Fig. S11: Expanded view of ESI-MS spectrum of $Zn(NO_3)_2$ and 2-methylimidazole mixture (1:2 molar ratio) after 2 hours of mixing.

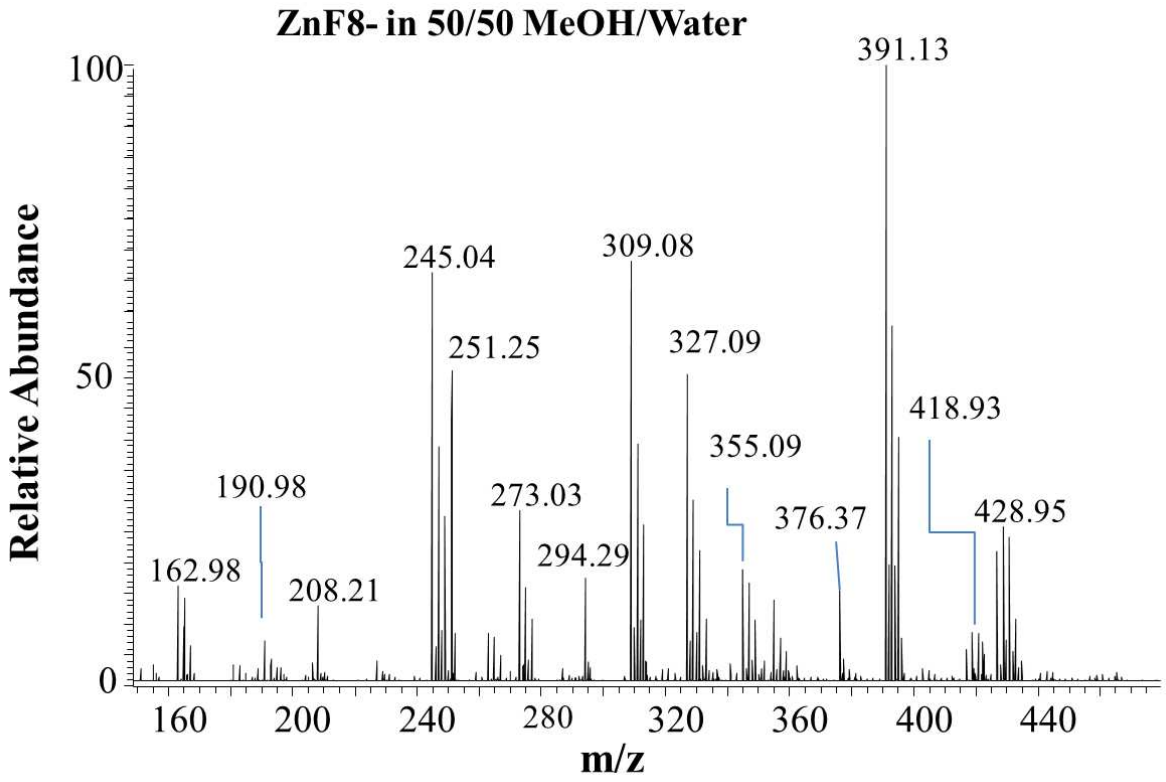

Fig. S12. ESI-MS spectrum of as-synthesized ZIF-8 dispersed in water/methanol (1:1 v/v) solution. We also explored the mass spectrum of the as-synthesized ZIF-8 by dispersing it in a methanol/water (50:50) at a sufficiently low concentration such that it forms a colloidal suspension and therefore can be electro-sprayed from the solution. This shows the mass spectrum with ions corresponding to Zn (*2-mim*)$_x$. (*2-mim*-H)$^+$ as well as their hydrated counterparts. We also observe some ion where x = 5-7, but these are of much lower abundances.

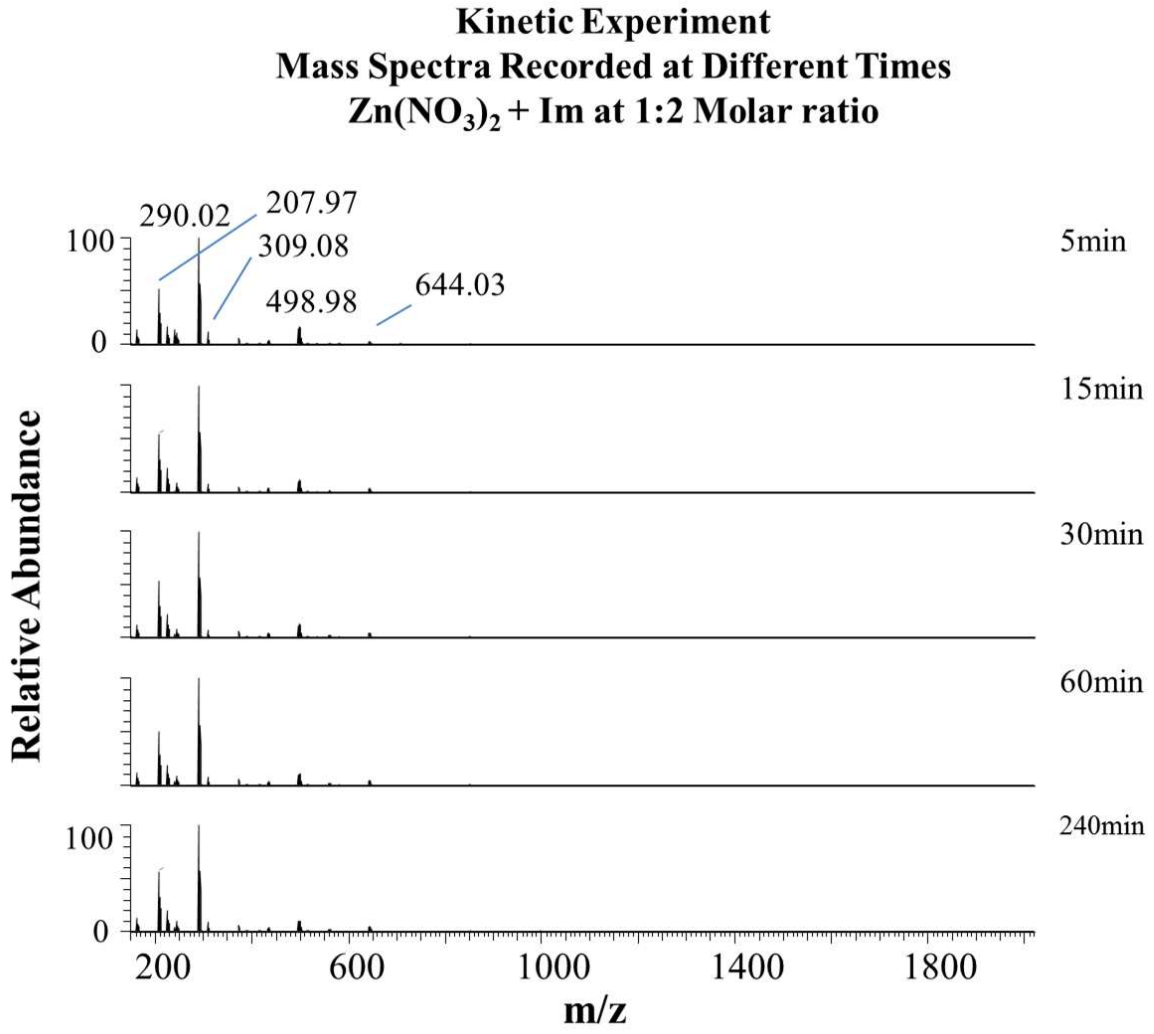

Fig. S13: Time dependent ESI-MS spectrum of $Zn(NO_3)_2$ and 2-methylimidazole mixture in 1:2 molar ratio (from top to bottom) – 5 min, 15 min, 30 min, 60 min and 240 min. Qualitatively, no changes are observed over time.

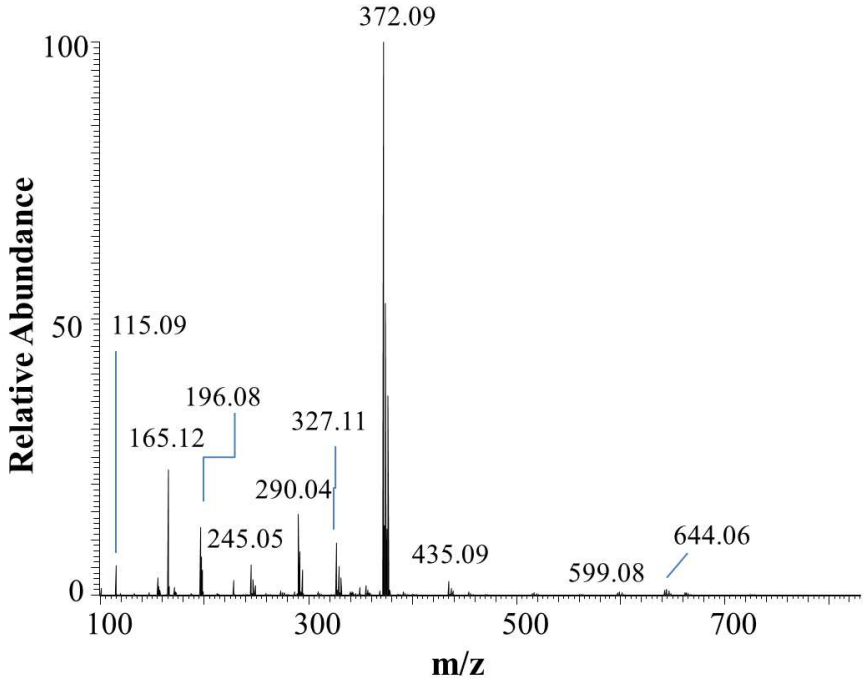

Fig. S14: Larger view of Full ESI-MS spectrum of $Zn(NO_3)_2$ and 2-methylimidazole mixture (1:2 molar ratio).

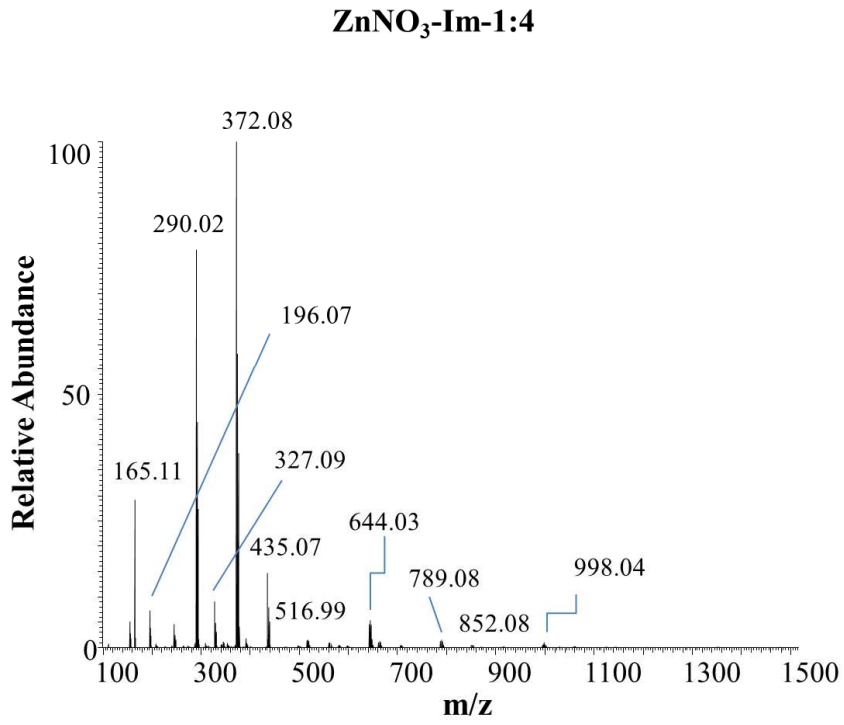

Fig. S15: Larger view of **f**ull ESI-MS spectrum of $Zn(NO_3)_2$ and 2-methylimidazole mixture (1:4 molar ratio).

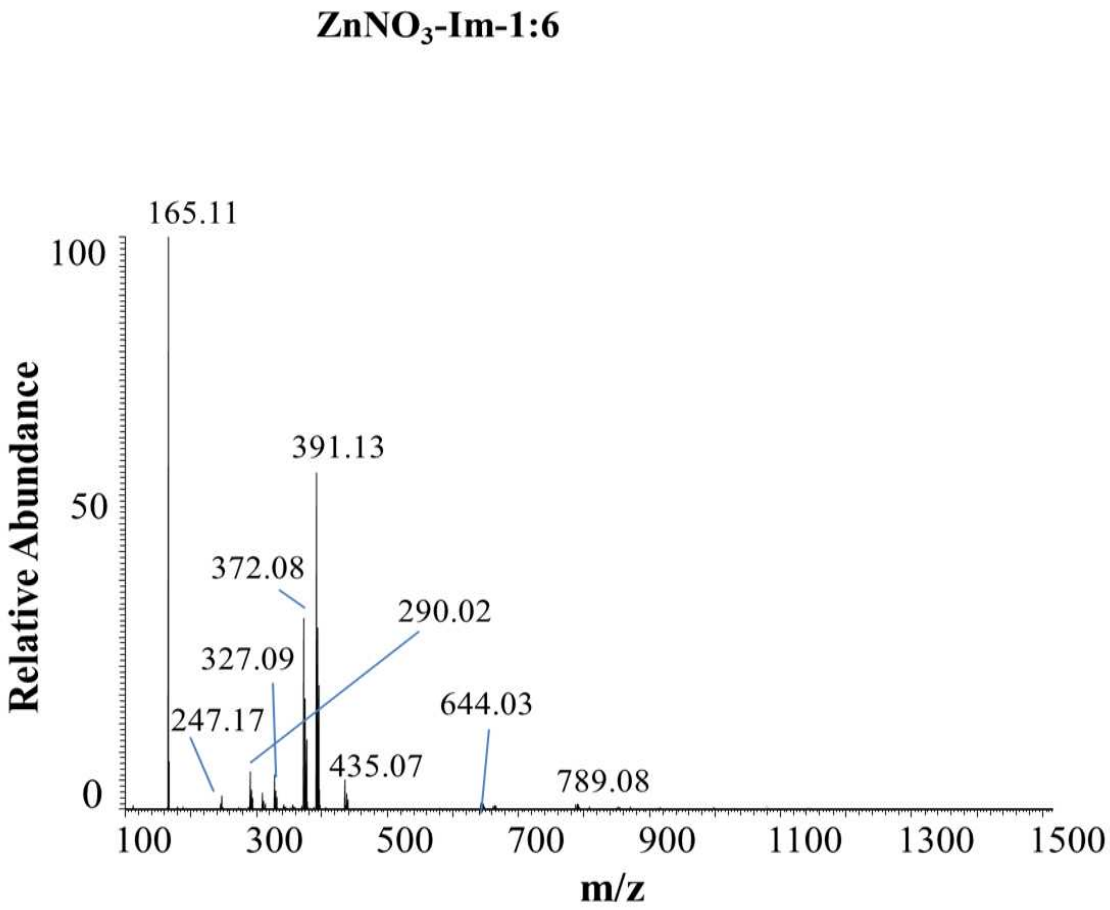

Fig. S16: Larger view of **f**ull ESI-MS spectrum of $Zn(NO_3)_2$ and 2-methylimidazole mixture (1:6 molar ratio).

VI. **Liquid Time of Flight-Secondary Ion Mass Spectrometry (TOF-SIMS):**

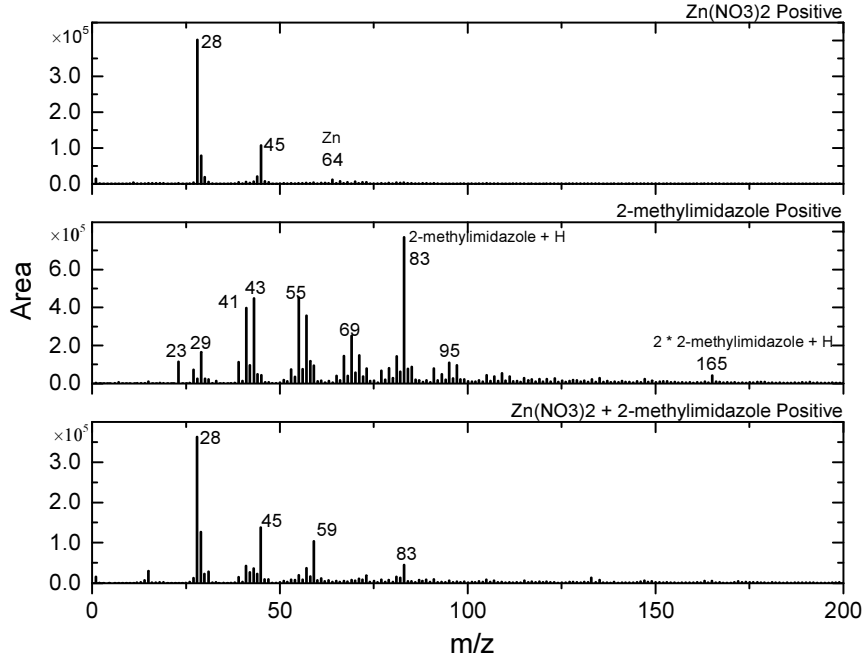

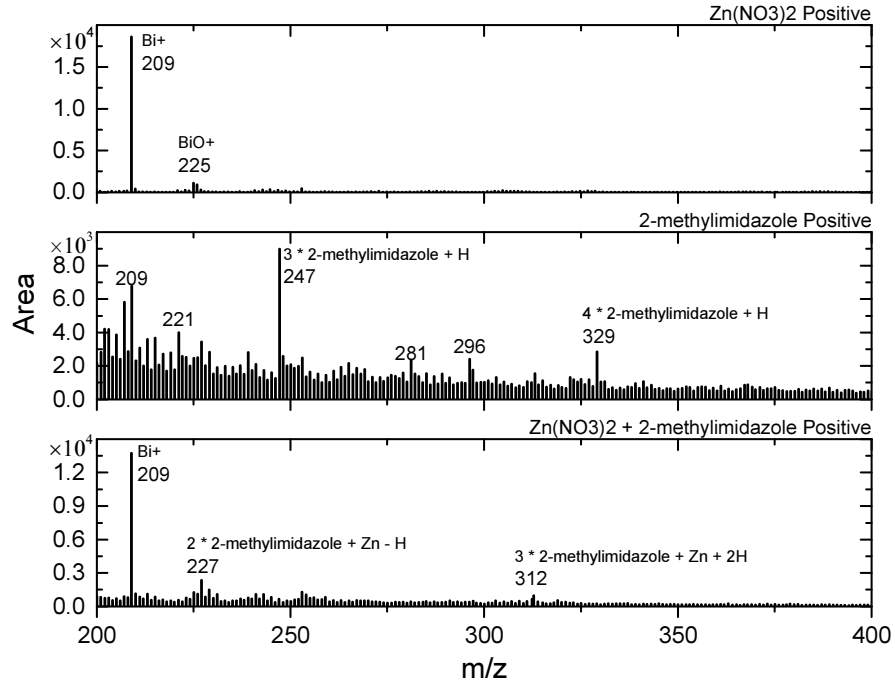

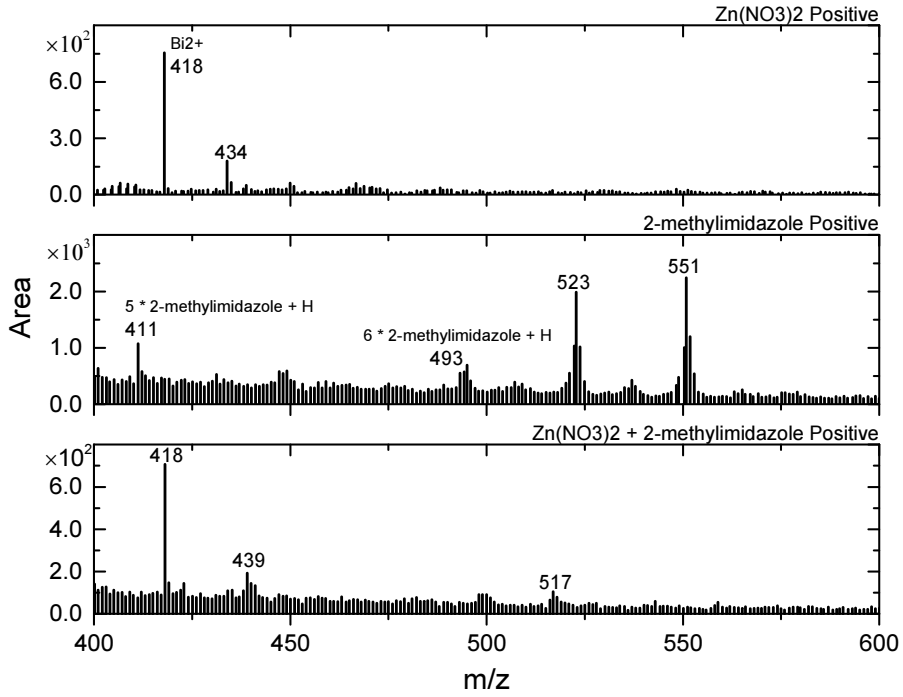

Fig. S17: *In situ* liquid-SIMS positive ion spectra of a $Zn(NO_3)_2$ solution sample, a *2-mim* solution sample, and a mixed $Zn(NO_3)_2$ and *2-mim* solution sample in a mass range of m/z 0-600. The spectrum of a *2-mim* solution sample shows very clear $[(2\text{-}mim)_n+H]^+$ monomer and cluster peaks (m/z 83, 165, 247, 329, 411 and 493), indicating formation of $(2\text{-}mim)_n$ clusters (n = 1-6) in the solution. As a comparison, the $(2\text{-}mim)_n$ cluster peaks in the spectrum of the mixed sample become much weaker, indicating dissociation of $(2\text{-}mim)_n$ clusters and formation of ZIF-8 MOF structure..

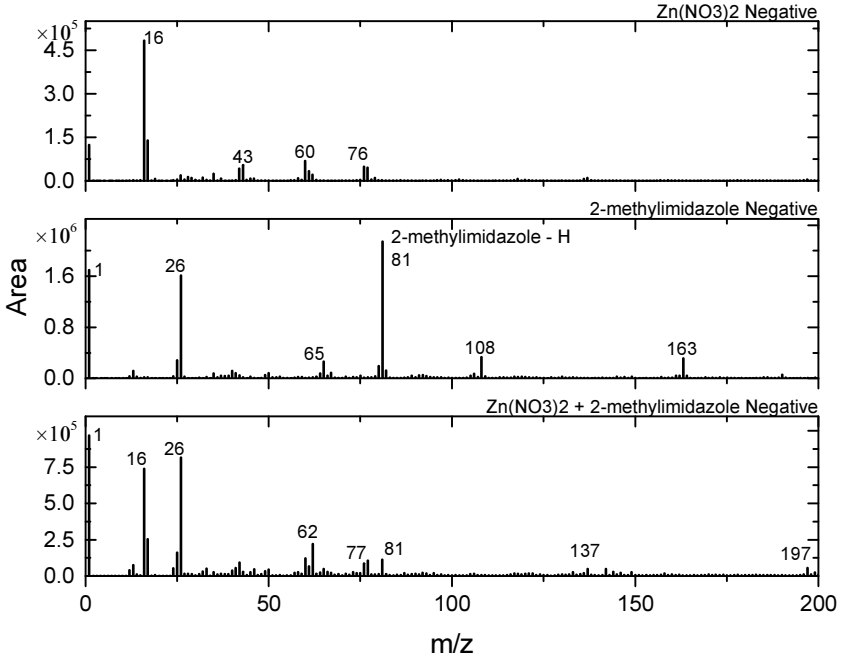
Zn(NO3)2 Negative
×10^5
4.5
3.0
1.5
0.0
16
43
60
76
2-methylimidazole Negative
×10^6
1.6
0.8
0.0
1
26
2-methylimidazole - H
81
65
108
163
Zn(NO3)2 + 2-methylimidazole Negative
×10^5
7.5
5.0
2.5
0.0
1
16
26
62
77
81
137
197
Area
0
50
100
150
200
m/z

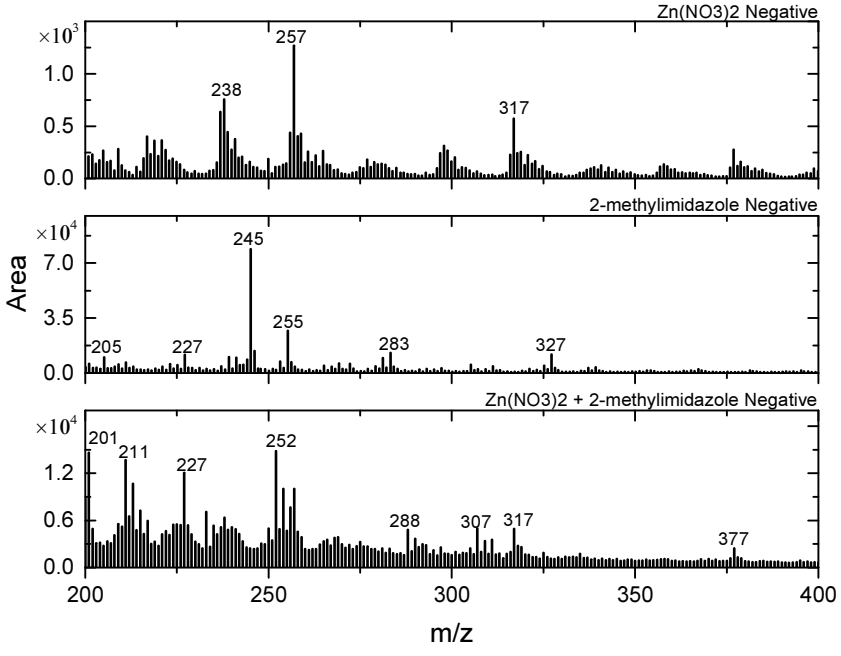
Zn(NO3)2 Negative
×10^3
1.0
0.5
0.0
257
238
317
2-methylimidazole Negative
×10^4
7.0
3.5
0.0
245
255
205
227
283
327
Zn(NO3)2 + 2-methylimidazole Negative
×10^4
1.2
0.6
0.0
201
211
227
252
288
307
317
377
Area
200
250
300
350
400
m/z

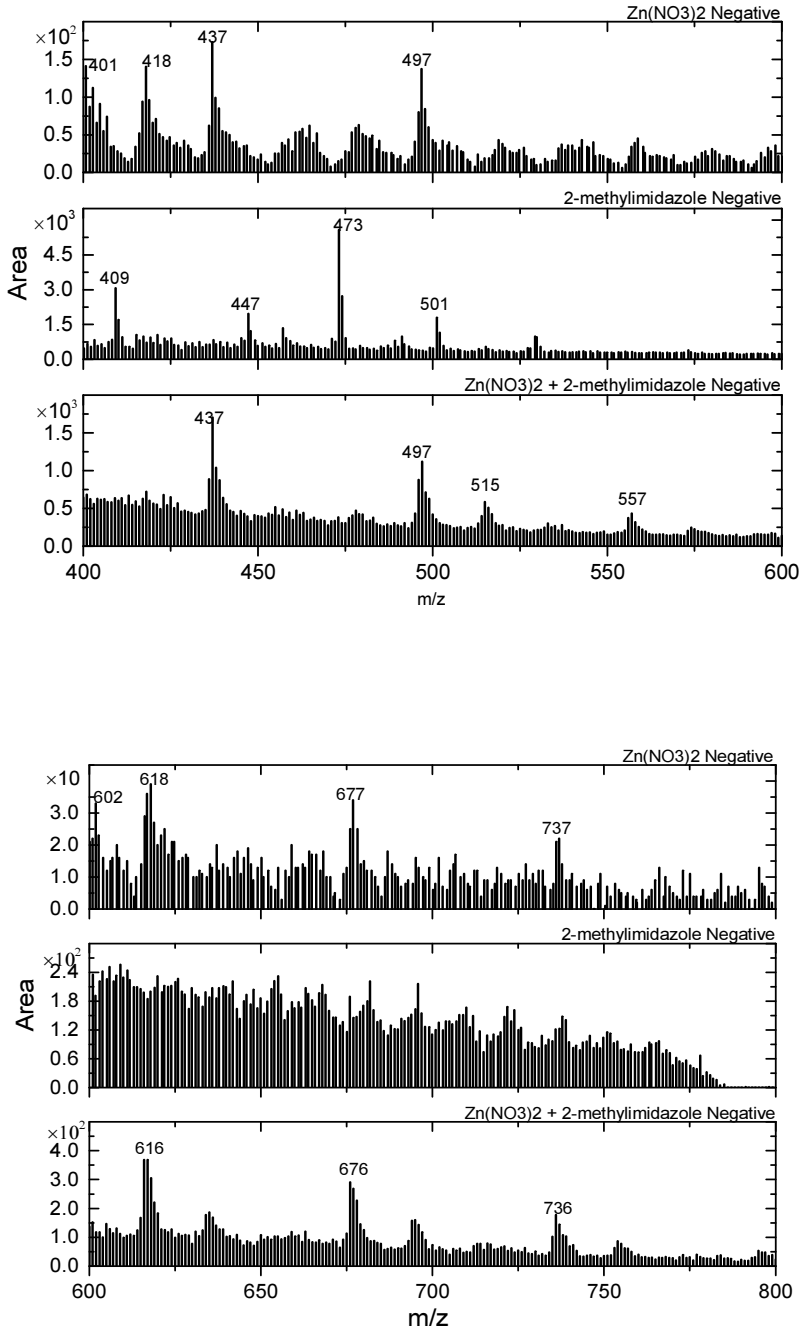

Fig. S18: *In situ* liquid-SIMS negative ion spectra of a $Zn(NO_3)_2$ solution sample, a *2-mim* solution sample, and a mixed $Zn(NO_3)_2$ and *2-mim* solution sample in a mass range of m/z 0-600. The spectrum of a *2-mim* solution sample shows very clear $[(2\text{-}mim)_n–H]^-$ monomer and cluster peaks (m/z 81, 163, 245, 327 and 409), indicating formation of $(2\text{-}mim)_n$ clusters (n = 1-5) in the solution. As a comparison, the $(2\text{-}mim)_n$ cluster peaks in the spectrum of the mixed sample become much weaker, indicating dissociation of $(2\text{-}mim)_n$ clusters and formation of ZIF-8 MOF structure.

VII. Computational methods:

DFT calculations on Zn(*2-mim*)$_x$ were performed using Gaussian basis sets with NWCHEM code.[6] We used PBE0 exchange-correlation functional,[7] a hybrid functional with 25% Hatree-Fock exchange energy. Recent studies indicate that PBE0 predicts performs well in predicting energetics and structure of organometallic complexes.[8] We used the Dunning's correlation consistent polarized basis sets augmented with diffuse functions at the level of aug-cc-pVDZ as supplied in NWCHEM.[9] To minimize computational complexity, diffuse functions were added only for the Zn species. Grimme's DFT-D3 dispersion was accounted for when computing the energetics.[10,11] The molecules were optimized with the default convergence parameters of NWCHEM.

Table S1: Binding Energies of the Zn2+-(2-mim3)-4 and Co2+(2-mim)3-4

Structure	Binding Energy (BE) (kCal/mol)	BSSE (kCal/mol)	BSSE corrected BE (kCal/mol)
[1] Zn^{2+}.(2-mim$_4$)-a	-448.50	-3.71	-444.79
Zn^{2+}.(2-mim$_4$)-b	-417.11	-12.96	-404.15
Zn^{2+}.(2-mim$_4$)-c	-441.01	-13.82	-427.19
Zn^{2+}(2-mim$_3$)-a	-404.61	-11.01	-393.60
Zn^{2+}.(2-mim$_3$)-b	-377.22	-10.08	-367.13

For Zn(2-mim$_4$)$^{2+}$, aug-cc-pvdz basis set is used for all the atoms. Hence the BSSE error is lower.[5]

Binding energies are calculated using the formula $BE = E_{complex} - E_{metal} - \sum E_i$, where $E_{complex}$ is the energy of the molecule, E_{metal} is the energy of isolated metal atom and E_i is the energy of i^{th} imidazole monomer. Basis set superposition error (BSSE) is calculated as $\sum E_i^{ext} - E_i^{iso}$, where E_i^{ext} is the energy of the 2methyl imidazole ring with the extended basis set of the whole molecule and E_i^{iso} is the energy of the 2methyl imidazole ring with the standalone basis set.

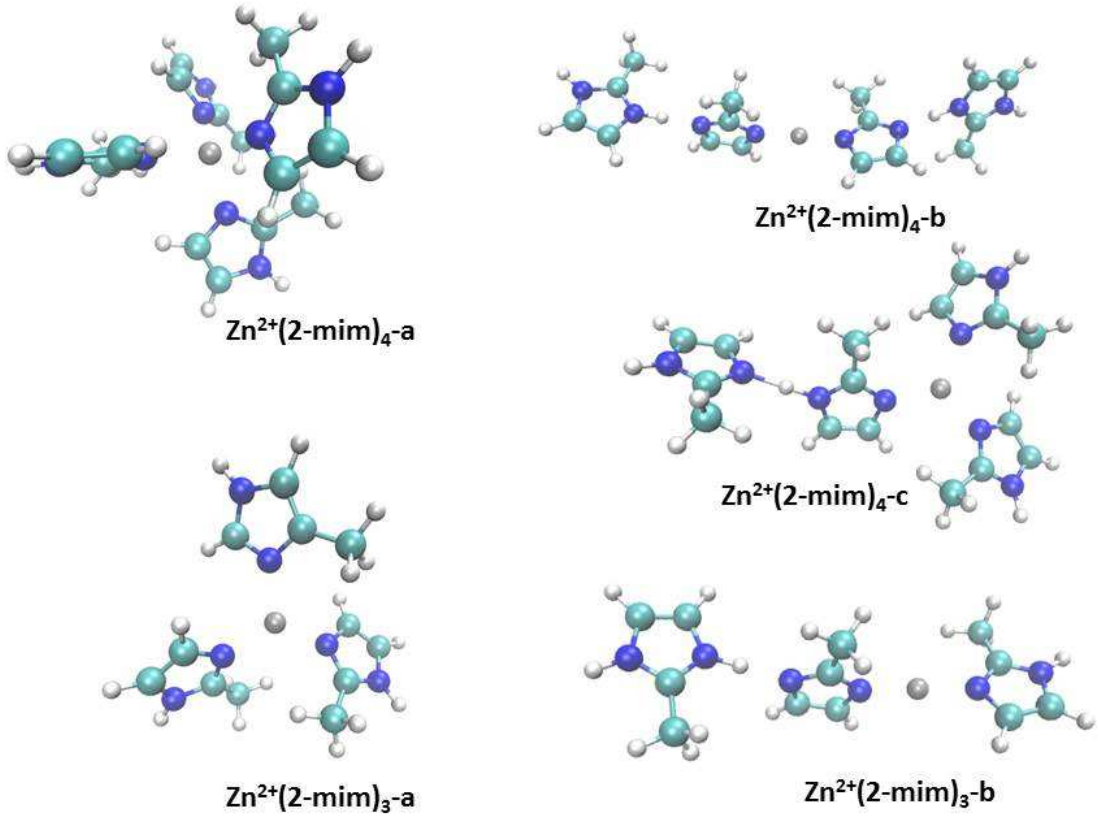

Fig. S19: Optimized $Zn^{2+}(2\text{-mim})_4$ structures

Table S2: Zn-N bond lengths in the lowest energy $[Zn(2\text{-mim})_4]^{2+}$ structure

Structure	Bond length (Å)
$Zn^{2+}.(2\text{-mim})_4$	2.017
	2.009
	2.013
	2.014

Table S3: Coordinates (in Å) of the lowest energy $Zn^{2+}.(2\text{-mim})_4$ structure

Zn	-0.01580401	0.00184295	0.04270875
C	-2.61793281	1.49825834	-0.60769094
C	-2.53730717	3.21715811	0.80256706
C	-1.41106195	2.46207008	0.94224143
N	-1.46880815	1.39633828	0.06036190
C	-3.14089602	0.56099380	-1.63197633
H	-4.17363441	2.90276180	-0.52166197
H	-2.86856043	4.12242012	1.29630441
H	-0.56789853	2.60912367	1.60703476
N	-3.27475495	2.59322726	-0.17532755
C	0.69565428	-1.32029051	-2.62553012
C	-0.87632621	-2.37051910	-1.52421790
C	-0.65840580	-3.08455962	-2.66454784
N	0.33124957	-2.40620727	-3.33555695
H	0.73207047	-2.67800007	-4.22399312
C	1.72107830	-0.34002017	-3.05955904
H	-1.56969579	-2.56866770	-0.71541545
H	-1.10388265	-3.99527953	-3.04556600
N	-0.03128308	-1.27404288	-1.50891071
C	2.61469274	0.69296544	1.32782423
C	3.60371381	1.63077271	1.34066282
C	2.10474214	2.15731132	-0.21542817
N	1.68885226	1.02608821	0.35551316
H	2.49882016	-0.18356252	1.95286982
H	4.49753113	1.73235902	1.94385855
H	3.78952982	3.36339081	0.12016613
C	1.42688644	2.90863581	-1.30147972
N	3.26099292	2.53600394	0.36480616
C	0.26148645	-2.28692926	2.01633141
C	-1.27222509	-1.86343620	3.56928808
C	-1.30468032	-0.88451547	2.62103867
N	-0.34804095	-1.15625209	1.65996424
C	1.34307447	-2.98468515	1.27604429
H	-0.00278383	-3.56877522	3.65741349
H	-1.84752473	-2.01399738	4.47446954
H	-1.93914144	-0.00829495	2.56525667
N	-0.28272965	-2.72903245	3.16760472
H	1.76584426	-2.32147300	0.51448230
H	0.96077664	-3.88135666	0.76964810
H	2.14871189	-3.29743513	1.95122878
H	-3.69227365	1.09860595	-2.41180205
H	-3.82489662	-0.17072303	-1.17973900
H	-2.31558793	0.01648014	-2.10081097
H	2.08668271	3.03731136	-2.16896787
H	1.12316802	3.90671394	-0.95979134
H	0.52758009	2.37319617	-1.62036485
H	2.49328567	-0.82381581	-3.66756043
H	2.20153119	0.10762807	-2.18320583
H	1.26969297	0.46018313	-3.66251808

VIII. Additional measurements:

Freshly synthesized ZIF-8 was characterized using the powder X-ray diffraction, Thermogravimetric analysis and BET surface area measurements. The BET was conducted on a Quantachrome Autosorb 1 MP.

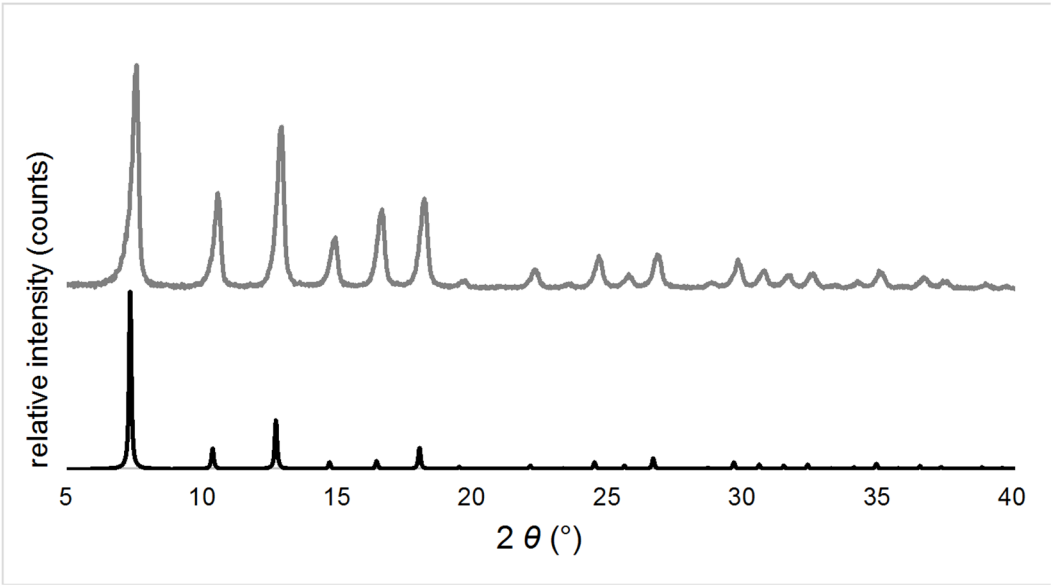

Fig. S20: Lab PXRD pattern of crystalline ZIF-8 (grey) compared to a simulated pattern (black) Cambridge Structural Database (CSD) reference FAWCEN03.

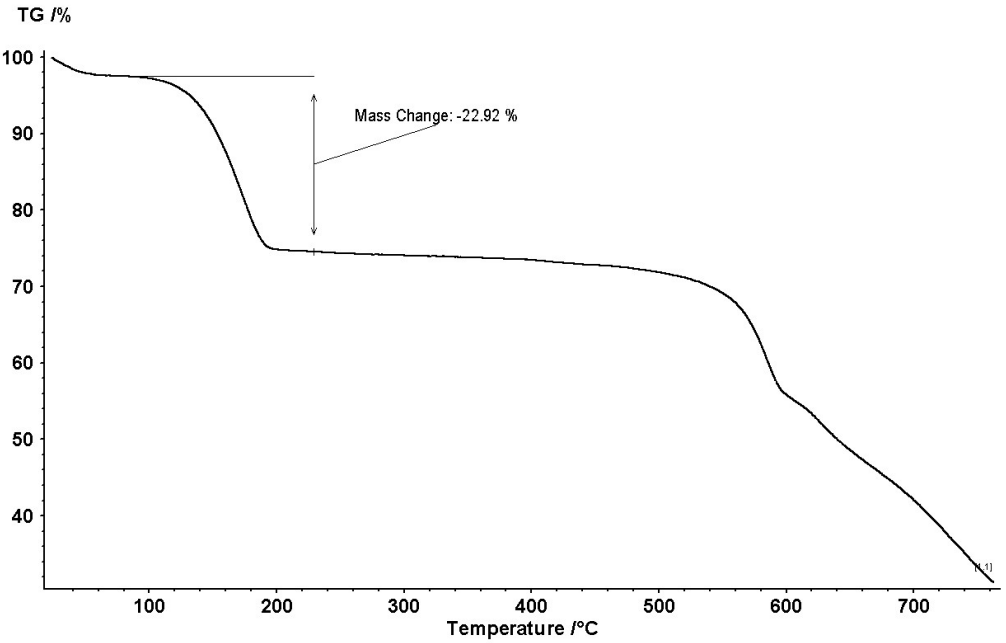

Fig. S21: Thermal gravimetric analysis (TGA) for ZIF-8.

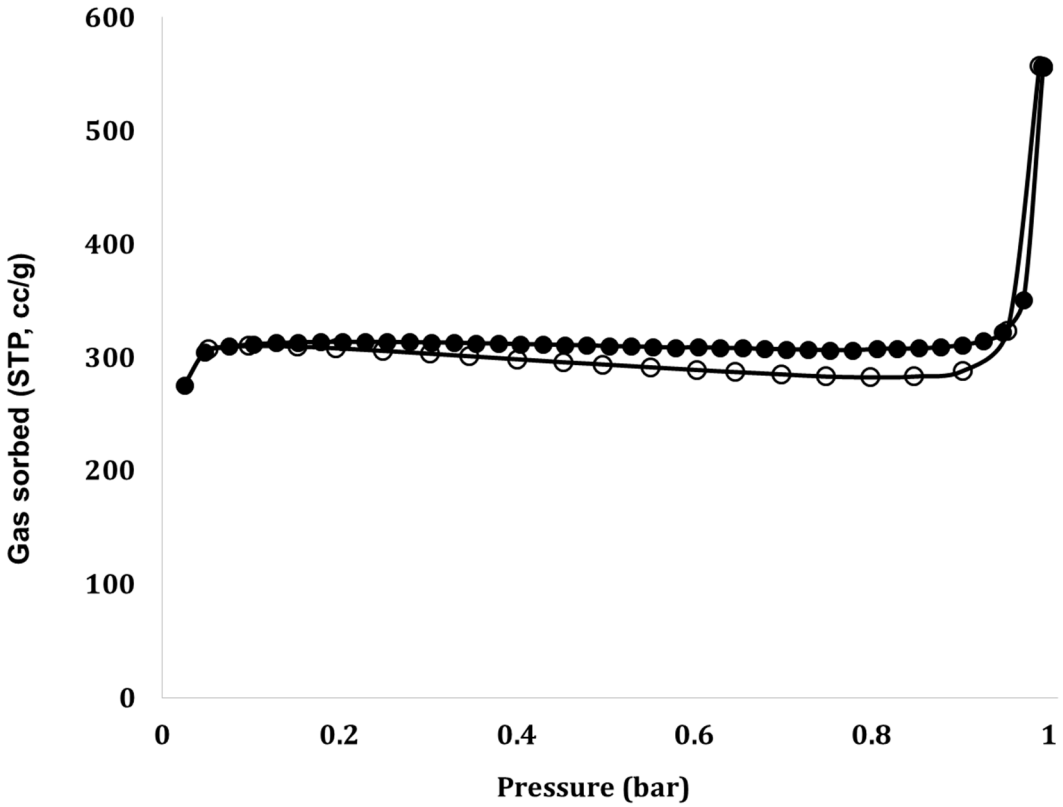

Fig. S22: Brunauer–Emmett–Teller (BET) surface area of ZIF-8 (958 m^2/g) using Nitrogen adsorption at 77K. **The solid and open circles indicate adsorption and desorption.**

Reference

(1) Farrow, C. L.; Billinge, S. J. L. Relationship between the atomic pair distribution function and small-angle scattering: implications for modeling of nanoparticles. *Acta Crystallographica a-Foundation and Advances* **2009**, *65*, 232-239.

(2) Kodama, K.; Iikubo, S.; Taguchi, T.; Shamoto, S. I. Finite size effects of nanoparticles on the atomic pair distribution functions. *Acta Crystallogr A* **2006**, *62*, 444-453.

(3) Farrow, C. L.; Juhas, P.; Liu, J. W.; Bryndin, D.; Bozin, E. S.; Bloch, J.; Proffen, T.; Billinge, S. J. L. PDFfit2 and PDFgui: computer programs for studying nanostructure in crystals. *Journal of Physics-Condensed Matter* **2007**, *19*.

(4) Jeong, I. K.; Proffen, T.; Mohiuddin-Jacobs, F.; Billinge, S. J. L. Measuring correlated atomic motion using X-ray diffraction. *J Phys Chem A* **1999**, *103*, 921-924.

(5) Juhas, P.; Farrow, C. L.; Yang, X. H.; Knox, K. R.; Billinge, S. J. L. Complex modeling: a strategy and software program for combining multiple information sources to solve ill posed structure and nanostructure inverse problems. *Acta Crystallographica a-Foundation and Advances* **2015**, *71*, 562-568.

(6) Valiev, M.; Bylaska, E. J.; Govind, N.; Kowalski, K.; Straatsma, T. P.; Van Dam, H. J. J.; Wang, D.; Nieplocha, J.; Apra, E.; Windus, T. L.; de Jong, W. NWChem: A comprehensive and scalable open-source solution for large scale molecular simulations. *Computer Physics Communications* **2010**, *181*, 1477-1489.

(7) Adamo, C.; Barone, V. Toward reliable density functional methods without adjustable parameters: The PBE0 model. *Journal of Chemical Physics* **1999**, *110*, 6158-6170.

(8) Rappoport, D.; Crawford, N. R. M.; Furche, F.; Burke, K.: Approximate Density Functionals: Which Should I Choose. In *Encyclopedia of Inorganic Chemistry*, 2009.

(9) Dunning, T. H. Gaussian-Basis Sets for Use in Correlated Molecular Calculations .1. The Atoms Boron through Neon and Hydrogen. *Journal of Chemical Physics* **1989**, *90*, 1007-1023.

(10) Grimme, S. Semiempirical hybrid density functional with perturbative second-order correlation. *Journal of Chemical Physics* **2006**, *124*.

(11) Grimme, S.; Antony, J.; Ehrlich, S.; Krieg, H. A consistent and accurate ab initio parametrization of density functional dispersion correction (DFT-D) for the 94 elements H-Pu. *Journal of Chemical Physics* **2010**, *132*.